JACS
JOURNAL OF THE AMERICAN CHEMICAL SOCIETY

Article

pubs.acs.org/JACS

Photoelectrochemical Hole Injection Revealed in Polyoxotitanate Nanocrystals Functionalized with Organic Adsorbates

Christian F. A. Negre,[†,▽] Karin J. Young,[†,∥,▽] Ma. Belén Oviedo,[‡] Laura J. Allen,[†,⊥] Cristián G. Sánchez,[¶] Katarzyna N. Jarzembska,[§,#] Jason B. Benedict,[§] Robert H. Crabtree,[†] Philip Coppens,*[,§] Gary W. Brudvig,*[,†] and Victor S. Batista*[,†]

[†]Department of Chemistry and Energy Sciences Institute, Yale University, P.O. Box 208107, New Haven, Connecticut 06520-8107, United States

[‡]Department of Chemistry, Drexel University, Philadelphia, Pennsylvania 19104, United States

[¶]Departamento de Matemática y Física, Facultad de Ciencias Químicas, INFIQC, Universidad Nacional de Córdoba, Ciudad Universitaria, X5000HUA, Córdoba, Argentina

[§]Department of Chemistry, University at Buffalo, State University of New York, Buffalo, New York 14260-3000, United States

[#]Department of Chemistry, University of Warsaw, Pasteura 1, 02-093, Warszawa, Poland

Supporting Information

ABSTRACT: We find that crystallographically resolved $Ti_{17}O_{24}(OPr^{i})_{20}$ nanoparticles, functionalized by covalent attachment of 4-nitrophenyl-acetylacetonate or coumarin 343 adsorbates, exhibit hole injection into surface states when photoexcited with visible light (λ = 400−680 nm). Our findings are supported by photoelectrochemical measurements, EPR spectroscopy, and quantum dynamics simulations of interfacial charge transfer. The underlying mechanism is consistent with measurements of photocathodic currents generated with visible light for thin layers of functionalized polyoxotitanate nanocrystals deposited on FTO working electrodes. The reported experimental and theoretical analysis demonstrates for the first time the feasibility of p-type sensitization of TiO_2 solely based on covalent binding of organic adsorbates.

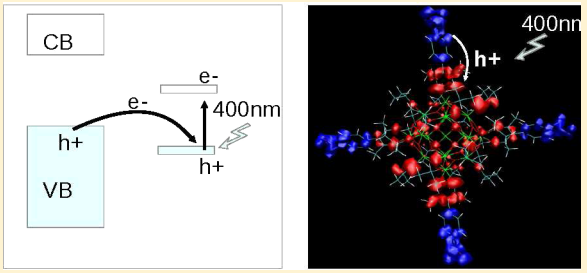

INTRODUCTION

Understanding the molecular mechanisms responsible for photoinduced interfacial charge transfer in functionalized semiconductor nanoparticles is a challenge of great current interest, critical to a wide range of photoelectrocatalytic applications and the development of efficient dye-sensitized solar cells (DSSCs).[1,2] The most common DSSCs (e.g., Grätzel cells) involve n-type sensitization of wide band gap semiconductors (e.g., TiO_2), based on covalent attachment of molecular dyes. On such surfaces, photoexcitation of the adsorbate dyes leads to electron injection into the conduction band (CB) of the semiconductor host substrate.[3−6] The circuit is typically completed by a redox relay couple (e.g., I^-/I_3^-) that regenerates the redox state of the dye and transfers the hole to the cathode. The photooxidized adsorbate (or the redox relay) might also advance the oxidation state of a catalyst in the electrolyte solution or coadsorbed on the photoanode surface for photocatalytic applications.[3,6,7] While n-type sensitization is a popular approach, we focus on another strategy that has been much less investigated and involves photoinduced hole injection into surface states of sensitized photocathodes.[8−12] Our data demonstrate p-type sensitization of polyoxotitanate nanoparticles by covalent binding of molecular adsorbates that introduce electronic states in the TiO_2 band gap, strongly mixed with the valence band.

Elucidating the mechanisms of interfacial charge transfer in functionalized metal oxide surfaces is challenging due to the complexity of the semiconductor/electrolyte interfaces and the lack of structural information at the molecular level.[4,5,13−23] Here, we overcome these challenges by focusing on polyoxotitanate (POT) nanocrystals with well-defined configurations as characterized by X-ray crystallographically. We analyze the dynamics of photoinduced charge separation by combining photoelectrochemical measurements, EPR spectroscopy, and quantum dynamics simulations.

Most of the studies of interfacial charge transfer in sensitized TiO_2 have been focused on anodic processes. Due to the high potential of the TiO_2 valence band, photocathodic processes have been much less investigated and usually limited to sensitization with high-valent transition metals.[11,24−27] Other materials investigated for photocatalytic reduction include p-type semiconductors, such as NiO, CuSCN, and CuI,[8−12,28] although fast recombination and limited hole diffusion often hinder charge separation in such

Received: September 8, 2014
Published: October 22, 2014

   dx.doi.org/10.1021/ja509270f | J. Am. Chem. Soc. 2014, 136, 16420−16429

semiconductor surfaces. Therefore, it is important to explore alternative materials, including hybrid semiconductor/organic interfaces for photocathodic applications. Here, we focus on POTs functionalized with organic dyes.

Detailed studies of electron and hole-injection mechanisms on semiconductor surfaces are difficult due to the variety of exposed crystal faces, absorption sites, and impurities present under typical experimental conditions. Our sensitized POTs, however, offer structurally resolved platforms for rigorous studies of charge transfer.[5,29] In particular, the nanocrystal $Ti_{17}O_{24}(OPr^i)_{20}$, called **$Ti_{17}$** throughout this manuscript, serves as a nanoparticulate building block for TiO_2 thin films of DSSCs. The cluster is small enough so that single crystals can be grown to determine the structure by using single crystal X-ray diffraction methods.

Previous computational studies of interfacial charge transfer in sensitized TiO_2 surfaces have been focused on the description of electron injection,[5,14−23] including simulations of the evolution of electronic excitations by interfacial electron transfer into the CB.[14] Computational methods included mixed quantum classical approaches in the wave packet picture as well as propagation schemes that evolved the density matrix according to the self-consistent DFTB Hamiltonian.[30] This kind of simulation, as implemented in our study, provides a description of the photoinduced charge transfer at the detailed molecular level, including an explicit treatment of the time-dependent electromagnetic field interaction with the sensitized surface.[31] The simulations thus account for electron−hole pair interactions during the interfacial charge-transfer process.

We focus on the analysis of hole and electron injection as a function of frequency of the perturbational field interacting with sensitized $Ti_{17}O_{24}(OPr^i)_{20}$ (Figure 1). The nanoclusters are capped with isopropoxide moieties and sensitized with **NPA** or **C343** to form sensitized **$Ti_{17}NPA_4$** = $Ti_{17}O_{24}(OPr^i)_{16}(NPA)_4$ and **$Ti_{17}C343_2$** = $Ti_{17}O_{24}(OPr^i)_{18}(C343)_2$) nanoparticles. The light-induced charge-separated states are probed by EPR spectroscopy and characterized by simulations of time-dependent photoinjection where both holes and electrons are studied by time-dependent DFTB. Using these methods, the IET mechanism can be rationalized based on the analysis of both static and time-dependent molecular orbital populations in conjunction with photoelectrochemical measurements and EPR spectroscopy. The combined characterization is confirmed by measurements of the photocathodic current generated by photoexcitation at 400−680 nm, as tested by using Grätzel-type cells with a thin layer of functionalized (**Ti_{17}**) deposited on the FTO working electrode. The resulting analysis demonstrates for the first time the feasibility of visible p-type sensitization of TiO_2 based on organic adsorbates, providing fundamental insights on the nature of structural and electronic factors that are essential for efficient photocathodic mechanisms in a wide range of applications.

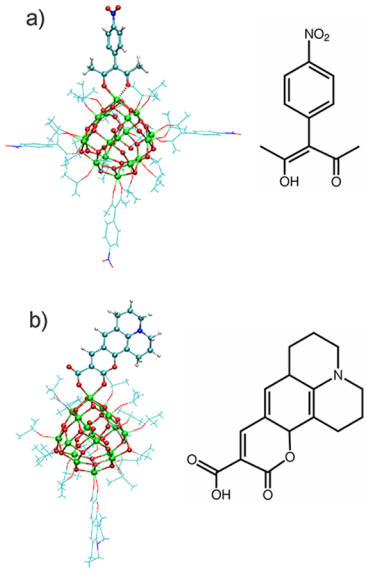

Figure 1. DFTB+ structural models: (a) **$Ti_{17}NPA_4$** ($Ti_{17}O_{24}(OPr^i)_{16}(NPA)_4$); (b) **$Ti_{17}C343_2$** ($Ti_{17}O_{24}(OPr^i)_{18}(C343)_2$). Color Key: Ti, green; O, red; C, cyan; N, blue; and H, white. **NPA** and **C343** ligands are schematically represented next to the corresponding nanoclusters.

EXPERIMENTAL AND COMPUTATIONAL METHODS

Materials Preparation. All reagents and solvents were purchased from commercial sources, while **$Ti_{17}NPA_4$** and **$Ti_{17}C343_2$** were prepared according to previously reported methods.[5] Benzene and dichloromethane were degassed, prior to transfer and storage in the glovebox. Because samples are very sensitive to hydrolysis in moist atmosphere with subsequent decomposition to TiO_2, all compounds containing titanium were stored and handled in a glovebox under nitrogen atmosphere. **$Ti_{17}NPA_4$** and **$Ti_{17}C343_2$** were stored in the dark to be protected from unnecessary exposure to light.

EPR Spectroscopy. Samples for EPR spectroscopy were prepared in a glovebox under N_2 atmosphere by dissolving 5 mg **$Ti_{17}NPA_4$** or **$Ti_{17}C343_2$** in 2 mL 1:1 dichloromethane:benzene and transferring approximately 200 μL of this sample to a 4 mm OD quartz EPR tube. Samples were frozen in liquid N_2 before being transferred to the cryostat. EPR spectra were measured at 7 K in perpendicular mode on a Bruker ELEXYS E500 spectrometer equipped with an SHQ cavity and Oxford ESR 900 liquid helium cryostat. Samples were illuminated in the cryostat at 7 K using a 1000 W Xe arc lamp equipped with a water filter and various long pass filters. Spectra were recorded with the following settings: microwave frequency = 9.3918 GHz, microwave power = 1.0 mW, modulation amplitude = 4 G, modulation frequency = 100 kHz.

Simulations of EPR Spectra. EPR spectra were simulated using EasySpin, version 4.0.0, for MATLAB R2009a. Spin systems for individual species were described by estimating *g*-values from the spectrum and refining empirically. Broadening was described using *g*-strain, meaning that the inhomogeneous broadening of the spectrum results from variations in the *g*-factor caused by similar but not identical environments of the unpaired electrons. The simulated experimental parameters included the microwave frequency (9.3918 GHz), temperature (7 K), and modulation amplitude (0.4 mT). Spectra were simulated using the EasySpin function pepper for solid-state CW EPR spectra. Basis spectra were calculated for each species and were scaled using an empirical scaling factor before being summed and compared to the experimental spectrum. Changes to the spin system parameters were made manually until a reasonable fit was achieved. Therefore, spin polarization was not explicitly treated in the fit to the EPR spectrum. Any hyperfine coupling to the protons on the organic radical was unresolved, and the broadening was treated using uncertainty in the *g*-value.

Photophysical Measurements. UV−vis absorbance spectra of **$Ti_{17}NPA_4$** and **$Ti_{17}C343_2$** were collected from dichloromethane solutions prepared in a glovebox and loaded into a quartz cuvette that was sealed with a Kontes valve. Spectra were collected using a Cary 50 UV−vis spectrophotometer in the range of 200−800 nm

dx.doi.org/10.1021/ja509270f | J. Am. Chem. Soc. 2014, 136, 16420−16429

with a scanning speed of 600 nm/min. All spectra were baseline corrected with the pure solvent spectrum.

Photoelectrochemistry. Short-circuit photocurrent action spectra were acquired using instrumentation described elsewhere.[6] A custom-made 500-μL Teflon cell with a sensitized FTO/$Ti_{17}NPA_4$ working electrode and a Pt mesh counter electrode was used. The electrolyte solution consisted of 0.05 M I_2 and 0.5 M LiI in CH_3CN.

Electronic Structure and Density Matrix Propagation. The electronic structure of model systems (cluster, molecule, and cluster-molecule) was described by a self-consistent density functional tight-binding Hamiltonian.[32] We employed the DFTB+ code to compute the Hamiltonian matrix elements and to achieve charge self-consistency.[33] The DFTB Hamiltonian matrix elements are defined as follows:

$$H^0_{\mu\nu} = \langle \varphi_\mu | \hat{H}_0 | \varphi_\nu \rangle + \frac{1}{2} S_{\mu\nu} \sum_X (\gamma_{AX} + \gamma_{BX}) \Delta q_X \tag{1}$$

where $S_{\mu\nu} = \langle \phi_\nu | \phi_\mu \rangle$ is the overlap matrix element between the localized atomic orbitals ϕ_μ and ϕ_ν of atoms A and B, respectively, $\Delta q_X = q_X - q^0_X$ is the change in Mulliken atomic charge of atom X, when comparing its charge when is part of the system (q_X) and its value in isolation (q^0_X). Matrix elements $\langle \phi_\mu | \hat{H}_0 | \phi_\nu \rangle$, $S_{\mu\nu}$, and γ_{AX} are parametrized as a function of interatomic distances, accounting implicitly for all interacting electron contributions. We have used the *tiorg-0-1* set of Slater–Koster parameters for Ti and O, while the *mio-0-1* set was used for the rest of the atoms. All the geometry optimizations were done at the DFTB level of theory as implemented in the DFTB+ code.

Our simulations of electron/hole injection dynamics involve quantum propagation of the one-electron density matrix $\rho = Cf(\epsilon)C^\dagger$, where C and ϵ are the eigenvectors and eigenvalues obtained by diagonalization of the Hamiltonian H, while $f(\epsilon)$ is the Fermi–Dirac distribution. The density matrix is propagated by integrating the Liouville–von Neumann[34,35] equation of motion:

$$\frac{\partial \rho}{\partial t} = -\frac{i}{\hbar}[H, \rho] \tag{2}$$

where $H(t) = H^0 + \mathbf{E}(t)\cdot\hat{\mu}$, is the Hamiltonian describing the system perturbed by the external electromagnetic field $\mathbf{E}(t)$. The time step integration was set to 4.84 attoseconds for all simulations and E_0 = 0.01 V/Å. Having propagated $\hat{\rho}(t)$, we compute the evolution of expectation values, as follows: $\langle A(t) \rangle = \mathrm{Tr}(\hat{\rho}(t)\hat{A})$, where $\hat{A}$ is the operator representing the property of interest. When expressed in the atomic basis set, the *trace operator* ($\mathrm{Tr}(\hat{\rho}\hat{A})$) takes the sum of the diagonal elements of a the matrix representation of $\hat{\rho}\hat{A}$. The time propagation of the single electron density matrix within a DFTB formalism is a practical methodology that has been implemented in previous studies for the description of phenomena such as charge transport, and photocurrent generation, or the response to strong laser fields in comparison to linear response methods.[36−43] The efficiency of the methodology is particularly attractive when compared to other real-time methods based on TDDFT.

Optical Properties. The methodology for calculating optical properties through propagation of $\hat{\rho}(t)$ and calculation of the frequency-dependent polarizability have been described in previous works.[44,45] In this section, we briefly discuss the methodology.

The time-dependent dipole moment of the system in the absence of any dissipative mechanism is calculated as follows: $\mu(t) = \sum_i q_i(t) r_i$, where the charges $q_i(t)$ are computed from the density matrix $\rho(t)$, and r_i is the atomic position. When the applied field is much smaller than the molecular electric field, the system is in the linear response regime,[46−49] and the dipole moment $\hat{\mu}$ can be expressed as the convolution between the applied electric field and the response function (polarizability α, or first-order susceptibility), as follows:

$$\langle \mu(t) \rangle = \int_0^\infty \alpha(t-\tau)\mathbf{E}(\tau)d\tau \tag{3}$$

or in frequency domain:

$$\langle \mu(\omega) \rangle = \alpha(\omega)\mathbf{E}(\omega) \tag{4}$$

with the following Cartesian components:

$$\begin{pmatrix} \mu_x(\omega) \\ \mu_y(\omega) \\ \mu_z(\omega) \end{pmatrix} = \begin{pmatrix} \alpha_{xx}(\omega) & \alpha_{xy}(\omega) & \alpha_{xz}(\omega) \\ \alpha_{yx}(\omega) & \alpha_{yy}(\omega) & \alpha_{yz}(\omega) \\ \alpha_{zx}(\omega) & \alpha_{zy}(\omega) & \alpha_{zz}(\omega) \end{pmatrix} \begin{pmatrix} E_x(\omega) \\ E_y(\omega) \\ E_z(\omega) \end{pmatrix} \tag{5}$$

Diagonalization of the matrix form of α gives three eigenvectors that indicate the principal polarizability axes (v_1, v_2, and v_3). The average polarizability can then be defined as $\bar{\alpha} = (\alpha_{v1} + \alpha_{v2} + \alpha_{v3})/3$, where α_{v1} is the polarizability along v_1 and similar for the other terms. The imaginary part of the average polarizability $\bar{\alpha}$ represents a measurable quantity which can be directly related to the photoabsorption cross section:

$$\sigma(\omega) = \frac{4\pi\omega}{c} I(\bar{\alpha}) \tag{6}$$

where c is the speed of light and $I(\bar{\alpha})$ is the imaginary part of the average polarizability. In the dynamical process, electrons can exchange energy among each other through the nonlinear self-consistent terms of the DFTB+ Hamiltonian. Other dissipative mechanisms have been neglected in the simulations, although they would be necessary for longer time simulations.

Electron Injection Simulation. Our simulations of photo-induced electron/hole injection were based on the DFTB methodology reported in previous studies.[30,31] The photoinduced dynamics was triggered by application of a sinusoidal perturbation (laser excitation) $H(t) = H^0 + \mathbf{E}^0 \sin(\omega t)\cdot\hat{\mu}$, with frequency ω tuned to the adsorbate HOMO–LUMO transition. The injection rate was monitored by computing the time-dependent Mulliken atomic charges and by projecting the time-dependent density matrix onto the molecular orbital basis set. The diagonal elements of the projected density matrix represent the molecular orbital populations, while off-diagonal elements describe the electronic coherences. An advantage of our approach, based on the density matrix formalism along with the use of a self-consistent Hamiltonian, is that the method allows for the explicit description of electron–hole interactions.

RESULTS

EPR Characterization of Charge Separation. Figure 2 shows the light-*minus*-dark EPR spectra of **Ti_{17}NPA$_4$** (top)[5] and **Ti_{17}C343$_2$** (bottom) probing a paramagnetic charge-separated state generated by photoexcitation of the system. The spectra indicate multiple contributions from charge-separated states that belong primarily to Ti^{3+} centers, oxygen-centered radicals, and organic radicals. In general, signals at $g > 2$ derive from oxygen anion holes, and those at $g < 2$ are assigned to Ti^{3+} electrons, consistent with previous reports of charge separations in TiO_2. For example, a similar paramagnetic charge-separated state was observed when **Ti_{17}** particles were illuminated at low temperature.[5] The onset wavelength of excitation of the **Ti_{17}** particle was between 295 and 345 nm and shifted toward the visible when the **Ti_{17}** core was functionalized with **NPA**.

Assignment of EPR spectra. The structure and stoichiometry of each nanoparticles are known from our own X-ray diffraction data. Therefore, it is possible to analyze the EPR spectrum and assign the various contributions from different charge-separated states. The assignment of superimposed signals, however, requires simulation of the basis spectra that are added to reproduce the experimental data.

We start with the spectrum of unfunctionalized **Ti_{17}**, which can be reproduced by the combined spectra of three Ti^{3+} centers, three different oxygen-centered radicals, and a broad,

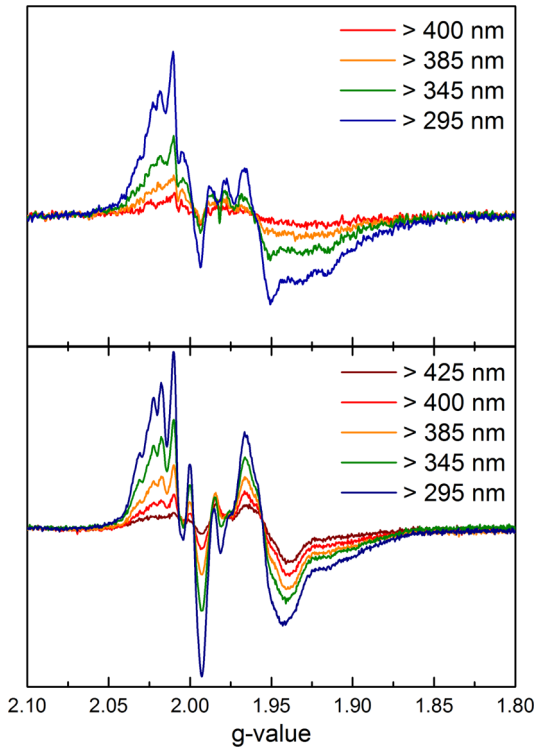

Figure 2. Light-*minus*-dark EPR spectra of $\mathbf{Ti_{17}NPA_4}$ (top)[5] and $\mathbf{Ti_{17}C343_2}$ (bottom) in frozen dichloromethane at 7 K. The illumination wavelengths were varied with long-λ pass filters.

isotropic background signal (Figure 3). The *g*-values of the three titanium signals, shown in Table 1, are comparable to those observed for anatase or rutile TiO_2.

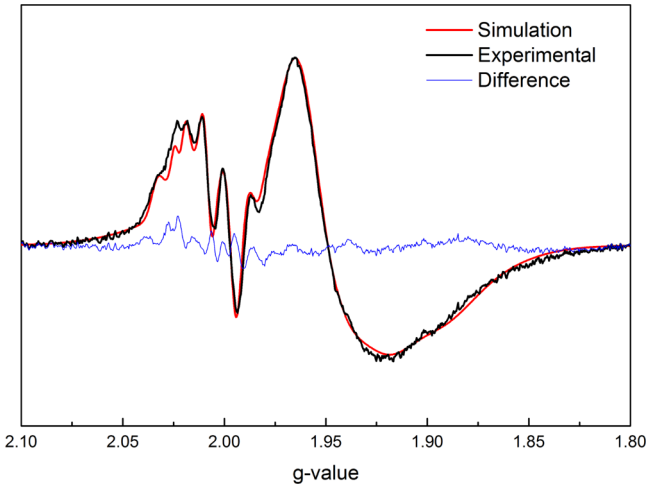

Figure 3. Light-*minus*-dark EPR spectra of unfunctionalized $\mathbf{Ti_{17}}$[5] in frozen dichloromethane solution at 7 K illuminated at λ > 295 nm. The sum of the simulated basis spectra (red) is compared to the experimental spectrum (black). The difference between the experimental and simulated spectra is shown in blue.

The Ti1 component is assigned to the four reactive five-coordinate centers in $\mathbf{Ti_{17}}$ because it changes when coordinated by photosensitizers, as described below. The three oxygen-centered radicals are similar to those assigned to oxygen-centered radicals in TiO_2. In addition, a broad isotropic signal at 1.945 is required to fit the overall spectrum. The origin of this species is uncertain, though the *g*-value suggests that it may correspond to Ti, analogous to EPR signals of bulk TiO_2 where isotropic background signals are typically observed and ascribed to surface Ti centers.[50]

In a previously reported NMR experiment in which the oxygen atoms in $\mathbf{Ti_{17}}$ were replaced by ^{17}O, four NMR signals were observed, suggesting that there are four types of oxygen present in $\mathbf{Ti_{17}}$.[51] One type is the oxygen in the isopropoxide capping groups, and the remaining are bridging oxos in the cluster. The contribution from oxygen-centered holes was represented by three rhombic signals in the simulation, suggesting that only three of the four types form stable radicals or that two of the lattice oxygen types have very similar *g*-values. Micic et al. have identified the *g*-values of lattice $O^{\bullet-}$ in colloidal aqueous TiO_2 as g_z = 2.0073, g_y = 2.0188, g_x = 2.0273,[52] which are comparable to the simulated values for O1. It is unexpected that O2 and O3 are simulated with *g*-values slightly below g_e, though O2 (g_z = 1.994) is close enough so the shift may represent the combined uncertainty of calculating the *g*-values and simulations. However, O3 is significantly different from what would be expected for a lattice oxygen radical. In a previous report of TiO_2 colloids prepared in methanol, a rhombic signal centered at $g_y \simeq 2.000$ was assigned to a methanol radical but was not discussed in detail.[52] By analogy, O3 may be related to radical formation on the capping isopropoxide groups. While hyperfine coupling to the C–H protons would be expected in such a species, it is possible that this coupling is not resolved in the spectrum of $\mathbf{Ti_{17}}$. In a similar study of TiO_2 chelated by mercapto-carboxylate ligands, a signal was observed above 150 K with g_x = 2.013, g_y = 1.976, g_z = 1.907 and assigned to "trapped electrons".[53] It may be possible that O3 is related to similar trapped electrons in these small particles. The species observed for the unfunctionalized $\mathbf{Ti_{17}}$ particles serve as the basis for comparison to the functionalized particles.

The EPR spectrum of $\mathbf{Ti_{17}}$ changes upon binding of **C343** or **NPA**, reflecting a change in the coordination environment of O and Ti centers (Figure 4).

As in the unfunctionalized nanoparticle, the same oxygen-centered species are observed for $\mathbf{Ti_{17}C343_2}$ illuminated with λ > 345 nm (Table 2).

However, four Ti^{3+} species are required to reproduce the region of the spectrum at g < 2. Three of the species are the same as those observed for $\mathbf{Ti_{17}}$ (Ti1, Ti2, and Ti3). The additional species (Ti4) is assigned to the Ti center coordinated by **C343**. Furthermore, a small contribution from an isotropic species with g = 1.999 was required for the best fit of the spectrum which was assigned to an organic radical centered on the **C343** chromophore.

Similar species are observed in the EPR spectrum of $\mathbf{Ti_{17}NPA_4}$ illuminated with λ > 345 nm (Table 3). The Ti signal of reactive five-coordinate centers is replaced by a signal that resembles Ti4 in $\mathbf{Ti_{17}C343_2}$. The oxygen radicals are very similar, and an organic radical is simulated at g = 2.001.

Since no direct band gap excitation is observed in unfunctionalized $\mathbf{Ti_{17}}$ particles,[5] upon excitation with λ > 345 nm light, the charge separation in $\mathbf{Ti_{17}C343_2}$ or $\mathbf{Ti_{17}NPA_4}$ must be occurring by interfacial electron transfer. At longer (>400 nm) illumination wavelengths, the simulation of the $\mathbf{Ti_{17}C343_2}$ spectrum produces all of the same species only differing in ratios (Figure 5 and Table 4).

dx.doi.org/10.1021/ja509270f | J. Am. Chem. Soc. 2014, 136, 16420–16429

Table 1. Simulation Parameters for the EPR Spectrum of Ti_{17} Illuminated at >295 nm

	g_x or $g_\perp$	g_y	g_z or $g_\parallel$	g-strain x or $\perp$	g-strain y	g-strain z or $\parallel$	scale coefficient
Ti1	1.950		1.889	0.022		0.030	30
Ti2	1.984		1.948	0.007		0.008	1
Ti3	1.961		1.919	0.020		0.025	38
O1	2.008	2.023	2.033	0.007	0.004	0.007	4
O2	2.020	2.008	1.994	0.006	0.005	0.006	12
O3	2.005	1.997	1.984	0.006	0.006	0.006	5
background	1.945			0.095			300

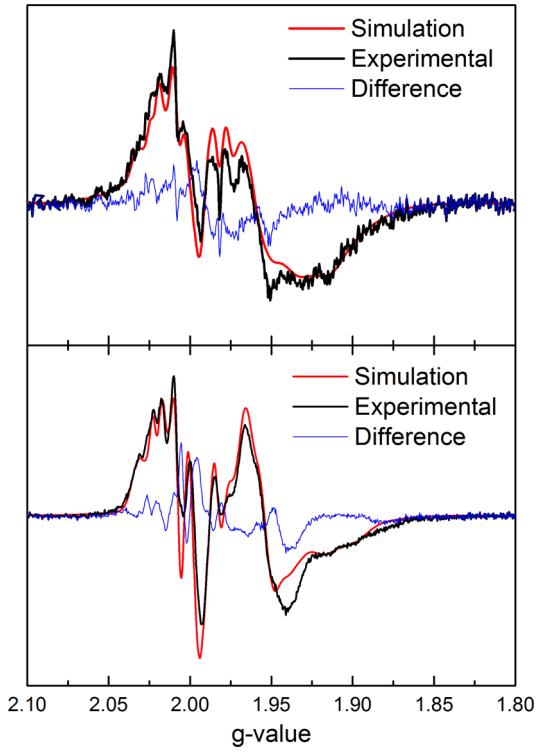

Figure 4. Simulation of the EPR spectra of $Ti_{17}NPA_4$ (top) and $Ti_{17}C343_2$ (bottom) illuminated with λ > 345 nm light. The sum of the simulated basis spectra (red) is compared to the experimental spectrum (black). The difference between the experimental and simulated spectra is in blue.

It is interesting to note, however, that the spectrum of $Ti_{17}NPA_4$ changes significantly when using the λ > 400 nm filter, as compared to the corresponding spectrum obtained with λ > 345 nm filter (Figure 5 and Table 5). When illuminated only with longer wavelengths, the spectrum of $Ti_{17}NPA_4$ includes a single type of oxygen-centered radical, an organic radical at g = 2.001, and a broad background signal at g = 1.959 similar to that observed for other POTs. The absence of Ti-centered signals suggests the absence of electron injection, while the signal characteristic of a hole on an oxygen center with an organic radical is suggestive of hole injection.

Simulations of Photoabsorption and Interfacial Electron Transfer. Figure 6 compares the experimental photoabsorption spectra for **C343** and $Ti_{17}C343_2$ to the calculated spectra obtained at the TD-DFTB level of theory. The computational structural models are based on the previously reported X-ray models of $Ti_{17}NPA_4$ and $Ti_{17}C343_2$,[5,54] optimized at the DFTB+ level. The relaxed geometries of the full systems are shown in Figure 1, and the comparison with the crystallographic structure as well as calculations of rmsd values are reported in the Supporting Information (SI). The favorable comparison of photoabsorption spectra partially validates the structural models for simulations of interfacial electron transfer.

Figure 7 shows the evolution of the time-dependent charge distribution in **C343** and Ti_{17}, upon photoexcitation of $Ti_{17}C343_2$ with a sinusoidal time-dependent electric field perturbation at 424 nm, tuned to the maximum of the lowest frequency band in the absorption spectrum (green arrow in Figure 6 b). Figure 7b shows that the adsorbate becomes increasingly negatively charged as a function of time.

Figure 8 shows that the corresponding absorption spectra for **NPA** and $Ti_{17}NPA_4$, with the maximum of **NPA** absorption in the lowest frequency band obtained at 386 nm (green arrow Figure 8b). Analogous to our findings with **C343**, photoabsorption at that low frequency band also induces charge separation and localizes negative charge on the chromophore, while the cluster becomes increasingly more positive (Figure 9b). These results are consistent with our experimental observations, based on EPR spectroscopy, suggesting that the charge-separated state involves hole injection from the adsorbate to the pseudoconduction band of the Ti_{17}, forming an anion radical on the adsorbate molecules.

Table 2. Simulation Parameters for the EPR Spectrum of $Ti_{17}C343_2$ Illuminated with λ > 345 nm

	g_x or $g_\perp$	g_y	g_z or $g_\parallel$	g-strain x or $\perp$	g-strain y	g-strain z or $\parallel$	scale coefficient
Ti1	1.956		1.889	0.011		0.018	80
Ti2	1.984		1.940	0.006		0.008	30
Ti3	1.965		1.917	0.011		0.018	80
Ti4	1.977		1.934	0.010		0.01	30
Org radical	1.999			0.009			10
O1	2.007	2.022	2.033	0.010	0.004	0.009	30
O2	2.019	2.008	1.995	0.006	0.005	0.007	70
O3	2.003	1.993	1.984	0.006	0.008	0.005	30
background	1.955			0.085			250

dx.doi.org/10.1021/ja509270f | J. Am. Chem. Soc. 2014, 136, 16420−16429

Table 3. Simulation Parameters for the EPR Spectrum of $Ti_{17}NPA_4$ Illuminated with $\lambda > 345$ nm

	g_x or $g_\perp$	g_y	g_z or $g_\parallel$	g-strain x or $\perp$	g-strain y	g-strain z or $\parallel$	scale coefficient
Ti1	1.977		1.933	0.006		0.010	2
Ti2	1.988		1.949	0.008		0.008	2
Ti3	1.964		1.912	0.015		0.015	12
Org radical	2.001			0.009			2
O1	2.007	2.023	2.033	0.009	0.004	0.007	3
O2	2.020	2.008	1.994	0.006	0.005	0.006	11
O3	2.005	1.994	1.982	0.004	0.006	0.004	3
background	1.960			0.080			200

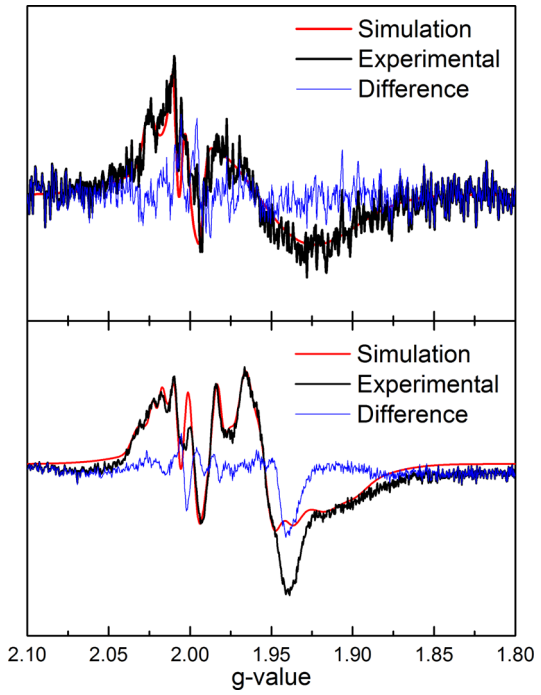

Figure 5. Simulation of the EPR spectra of $Ti_{17}NPA_4$ (top) and $Ti_{17}C343_2$ (bottom) illuminated with $\lambda > 400$ nm light. The sum of the simulated basis spectra (red) is compared to the experimental spectrum (black). The difference between the experimental and simulated spectra is in blue.

For completeness, we have also analyzed photoexcitation at higher frequencies, including photoexcitation at 263 nm for $Ti_{17}NPA_4$ and at 221 nm for $Ti_{17}C343_2$ (i.e., the second band in the absorption spectra, shown with magenta arrows in Figures 6b and 8b). At these shorter wavelengths, the Ti_{17} clusters becomes increasingly negative as a function of time, while the photosensitizer becomes increasingly positive (Figures 7a and 9a), consistent with electron transfer into the cluster upon photoexcitation of the chomophore.

To better understand the mechanism of hole injection and to compare the underlying dynamics of electron injection induced by higher frequency photons, we analyze the evolution of the electronic population of frontier orbitals that participate in the response to the external perturbational field. Figures 10 and 11 show the time-dependent population of electronic states in $Ti_{17}NPA_4$ and $Ti_{17}C343_2$, respectively. In both figures, panels a and b compare the population dynamics triggered by photoexcitation with high and low frequency fields, respectively. The analysis includes states that are initially populated (occupied) or unoccupied in the unperturbed system and that undergo significant changes in population upon photoexcitation of the system, including states localized in the Ti_{17} cluster, depicted in blue, or in the molecular adsorbates (**NPA**/**C343**), depicted in red. Figure 12 shows the states that undergo significant changes in population after photoexcitation of the systems with high (magenta dots) and low (green dots) frequency photons, within the manifold of states mixed with the valence and conduction bands. For comparison, the Fermi level (E_F) was set to 0.0 eV for all DOS plots. Figure 12 also shows that the pDOS onto Ti_{17} for both systems is in good agreement with previously reported DOS calculations for anatase TiO_2 (see SI).[55,56]

Figures 10 and 11 show that donor states, below the Fermi level (E_F), are initially fully occupied and become partially depleted upon photoexcitation, while acceptor states (above E_F) are initially depleted and become partially populated. Photoexcitation with high frequency photons leads to depletion of donor states that are mostly localized in the adsorbates, leading to population of acceptor states localized in the Ti_{17} cluster. The response to the external perturbational field is thus consistent with electron injection through a direct (type II) transition mechanism. In addition, some of the donor states belong to Ti_{17} indicating that the observed

Table 4. Simulation Parameters for EPR Spectrum of $Ti_{17}C343_2$ Illuminated with $\lambda > 400$ nm

	g_x or $g_\perp$	g_y	g_z or $g_\parallel$	g-strain x or $\perp$	g-strain y	g-strain z or $\parallel$	scale coefficient
Ti1	1.956		1.889	0.011		0.018	30
Ti2	1.983		1.938	0.006		0.008	12
Ti3	1.965		1.917	0.011		0.018	30
Ti4	1.977		1.934	0.010		0.010	13
Org radical	1.999			0.009			3
O1	2.007	2.022	2.033	0.010	0.004	0.009	7
O2	2.019	2.008	1.995	0.006	0.005	0.007	17
O3	2.003	1.993	1.984	0.006	0.008	0.005	9
background	1.955			0.085			200

dx.doi.org/10.1021/ja509270f | J. Am. Chem. Soc. 2014, 136, 16420−16429

Table 5. Simulation Parameters for the EPR Spectrum of $Ti_{17}NPA_4$ Illuminated with $\lambda > 400$ nm

	g_x or $g_\perp$	g_y	g_z or $g_\parallel$	g-strain x or $\perp$	g-strain y	g-strain z or $\parallel$	scale coefficient
Org radical	2.001			0.007			2
O2	2.026	2.009	1.994	0.008	0.004	0.005	18
background	1.959			0.085			300

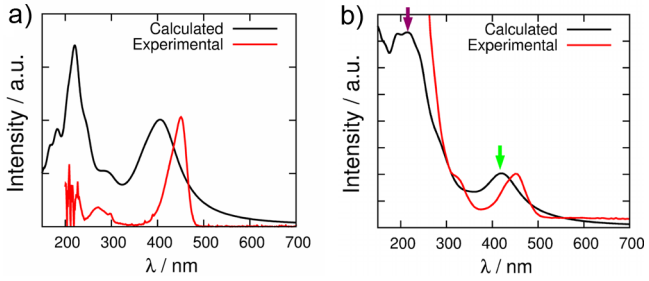

Figure 6. Simulated absorption spectrum for both free **C343** (a) and $Ti_{17}C343_2$ (b). Magenta and green arrows indicate the wavelengths at which electron and hole injection take place, respectively.

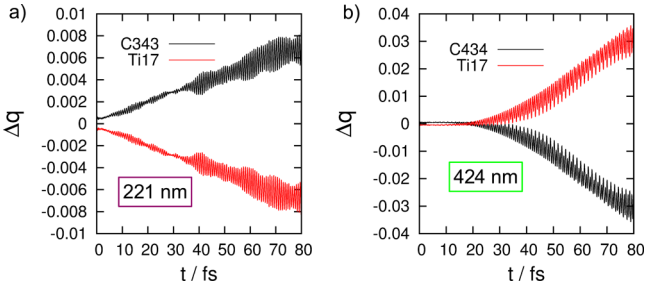

Figure 7. (a) Charge evolution during electron injection simulations at 221 nm on $Ti_{17}C343_2$ system. **C343** molecules show a gain in positive charge (black curve), while the Ti_{17} cluster gets negatively charged (red curve). (b) Charge evolution during electron injection simulation at 424 nm for $Ti_{17}C343_2$ system. The **C343** molecule shows a gain in negative charge (black curve), while the Ti_{17} cluster gets positively charged (red curve).

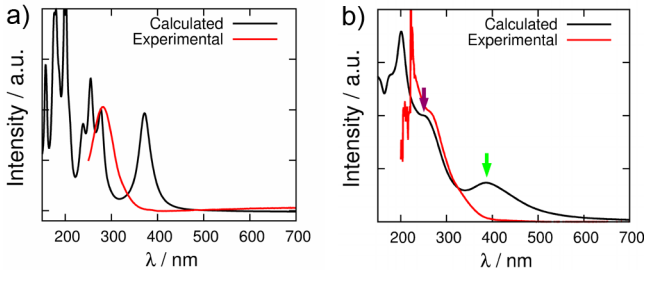

Figure 8. Simulated absorption spectrum for both free **NPA** (a) and $Ti_{17}NPA_4$ (b). Magenta and green arrows indicates the wavelengths at which electron and hole injection take place, respectively.

electron injection is mixed with direct interband transitions within the Ti_{17} cluster.

Photoexcitation of $Ti_{17}NPA_4$ at 386 nm triggers a mechanism with two fundamental steps, including a primary electronic excitation localized in the **NPA** adsorbate and a subsequent hole injection into the cluster. The hole injection refills the electronic state depopulated by the initial excitation (Figure 13), completing a photoexcitation process that effectively transfers an electron from surface states mixed

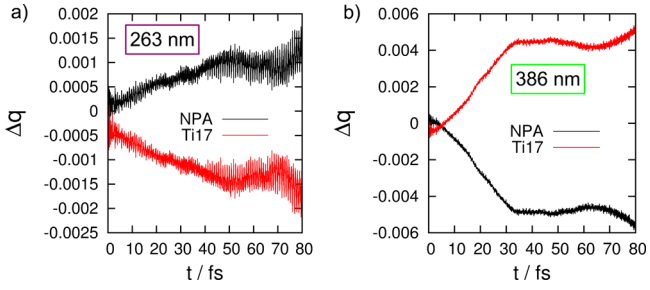

Figure 9. (a) Charge evolution during electron injection simulation at 263 nm on $Ti_{17}NPA_4$ system. **NPA** molecules show a gain of positive charge (black curve), while the Ti_{17} cluster becomes negatively charged (red curve). (b) Charge evolution during electron injection simulation at 386 nm for $Ti_{17}NPA_4$ system. The **NPA** molecule shows a gain in negative charge (black curve), while the Ti_{17} cluster gets positively charged (red curve).

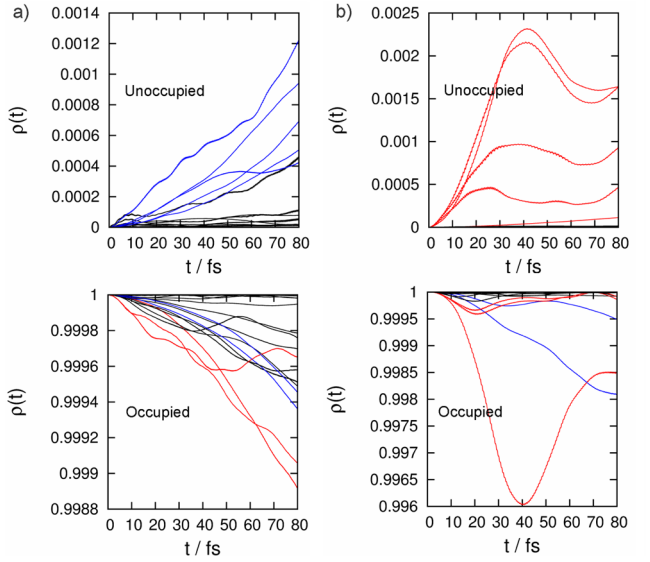

Figure 10. Occupied (bottom) and unoccupied (top) orbital population evolution for $Ti_{17}NPA_4$ during electron injection at (a) 263 and (b) 386 nm.

with the valence states of the semiconductor nanoparticles to the excited electronic state of adsorbate molecule.

For $Ti_{17}C343_2$, a similar response due to hole injection is induced by photoexcitation at 424 nm, while direct electron injection is observed upon excitation at higher energies (e.g., at 221 nm, as shown in Figure 14).

Experimental Confirmation of Hole Injection. We have tested the photoelectrochemical properties of the $Ti_{17}NPA_4$ complex, upon exposure to visible light, by assembling Grätzel-type photovoltaic solar cells with a thin layer of the complex deposited on an FTO working electrode. Exposure to light produces a cathodic current in the 400−680 nm wavelength range (see Figure 15), indicating hole injection and thus confirming the results of the calculation for exposure in this spectral region. The current is weak

dx.doi.org/10.1021/ja509270f | J. Am. Chem. Soc. 2014, 136, 16420−16429

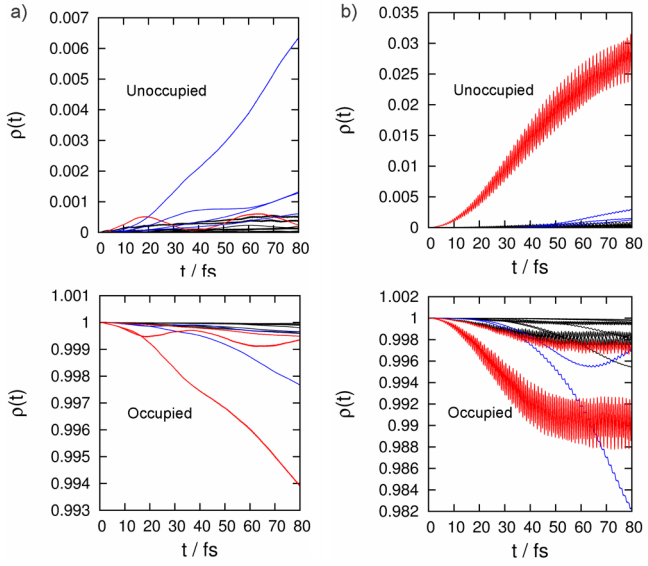

Figure 11. Occupied (bottom) and unoccupied (top) orbital population evolution for $\mathbf{Ti_{17}C343_2}$ during electron injection at (a) 221 and (b) 424 nm.

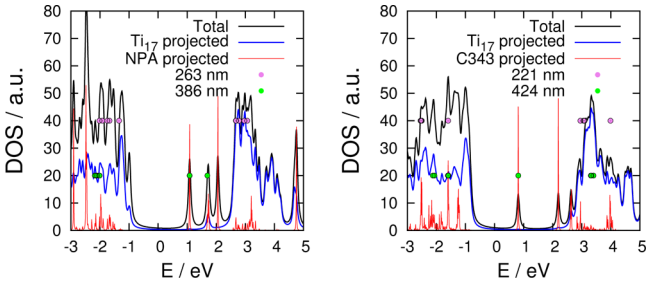

Figure 12. Left: DOS for $\mathbf{Ti_{17}NPA_4}$. Dots indicate the states that participate the most in the excitation. Right: DOS for $\mathbf{Ti_{17}C343_2}$. Very narrow Lorentzian functions of fwhm = 0.01 eV were employed for the projections onto the dyes, while 0.1 eV was used for the total and $\mathbf{Ti_{17}}$ projected DOS. The plots where shifted such that E_F = 0.0 eV.

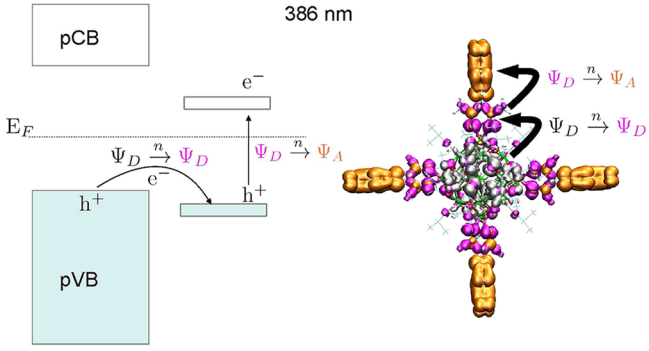

Figure 13. Scheme for hole injection. In this case, we have depicted the case of $\mathbf{Ti_{17}NPA_4}$ at 386 nm.

because of the low absorbance of the $\mathbf{Ti_{17}NPA_4}$ layer, the limited porosity of the polyoxotitanate sample, and the presence of the isopropoxy shell around the cluster surface which reduces charge transfer to the FTO electrode. Nevertheless, the results are fully reproducible, as shown in the figure for successive measurements. No response was recorded for a Ti_{17} reference sample.

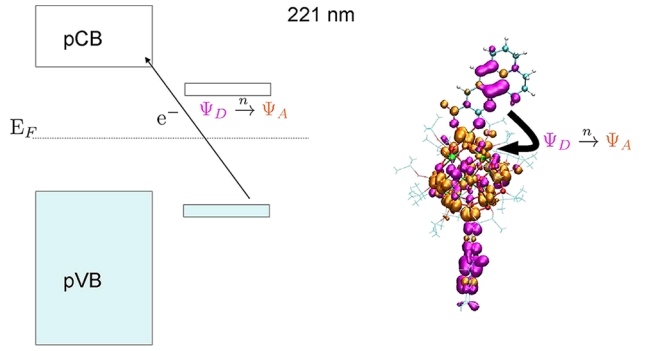

Figure 14. Scheme for electron injection. In this case we have depicted the case of $\mathbf{Ti_{17}C343_2}$ at 221 nm.

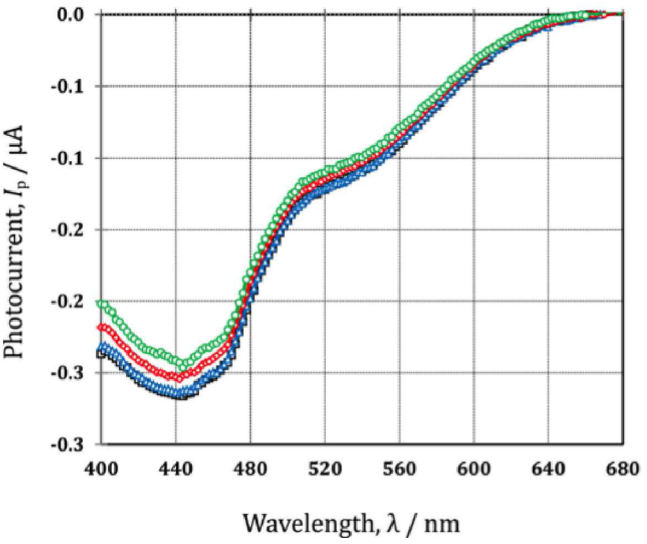

Figure 15. Negative (cathodic) photocurrent recorded for $Ti_{17}NPA_4$ supported by a FTO working electrode. Four successive measurements are shown.

DISCUSSION

EPR and photocurrent measurements, in conjunction with simulations of interfacial hole transfer based on TD-DFTB calculations, represent truly complementary techniques for studying charge separations in sensitized POTs. EPR allows the assignment of various species generated by charge separation, including different signals observed for Ti^{3+}, $O^{\bullet-}$, and organic radicals under steady-state conditions. Photocurrent measurements quantify charge collection upon exposure to light in the 400−680 nm wavelength range, and TD-DFTB simulations of interfacial charge transfer allow for examination of the ultrafast charge-separation during the early time relaxation after photoexcitaiton of the system.

The EPR spectrum of $\mathbf{Ti_{17}NPA_4}$, under exposure to visible light (λ > 400 nm), shows only signals assigned to oxygen hole and organic radicals. These results are consistent with holes injected into the cluster as predicted by quantum dynamics simulations and the alignment of electronic states, showing that the **NPA** LUMO is not poised to inject into $\mathbf{Ti_{17}}$ acceptor states when excited at low frequency as also shown in previous work.[5] When the photoexcitation wavelength is changed to λ > 345 nm, the EPR spectrum includes species assigned to Ti^{3+}, suggesting electron injection from the **NPA** donor orbitals to the $\mathbf{Ti_{17}}$ pseudoconduction band.

dx.doi.org/10.1021/ja509270f | J. Am. Chem. Soc. 2014, 136, 16420−16429

Analogous Ti^{3+} EPR signals are observed for $\mathbf{Ti_{17}C343_2}$ when photoexcited with $\lambda > 345$ nm. The calculations predict pure hole injection upon photoexcitation with $\lambda = 424$ nm, although the EPR spectrum also shows Ti^{3+} signals when photoexciting with $\lambda > 425$ nm (Figure 2, bottom panel). The reason for this small discrepancy can be attributed to the offset of 50 nm when comparing experimental and theoretical photoabsorption bands. The calculations also suggest pure electron injection into the conduction band (i.e., without hole injection into state mixed with the valence band), at $\lambda < 221$ nm, while direct excitation of $\mathbf{Ti_{17}}$ is produced at $\lambda < 345$ nm. A similar electron to hole injection frequency-dependent transition has already been shown for ruthenium complexes by Furtado et al.[26] We note that in our nanocrystals, the position of the frontier orbitals could have a strong dependence on the adsorption geometry. One possible way to provide independent verification of the band alignment responsible for hole injection would be by cyclic voltammetry measurement of the complex and their components. Such measurements could directly probe the HOMO and LUMO positions of the $\mathbf{Ti_{17}}$ cluster and **C343** as well as changes that result from complex formation. In fact, we have performed some preliminary experiments on cyclic voltamperometry that will be reported elsewhere since multiple nonreversible redox features are observed and require a further detailed study.

CONCLUSIONS

We have characterized the mechanism for hole injection into surface states of functionalized polyoxotitanate nanocrystals by combining EPR spectroscopy, photocurrent measurements, and quantum dynamics simulations of interfacial charge transfer in crystallographically resolved $Ti_{17}O_{24}(OPr^i)_{20}$ nanoparticles ($\mathbf{Ti_{17}}$), sensitized with 4-nitrophenyl-acetylacetonate, or coumarin 343 (**C343**). We found that hole injection into surface states, mixed with the TiO_2 valence band, can be induced in $\mathbf{Ti_{17}NPA_4}$ and $\mathbf{Ti_{17}C343_2}$ by photoexcitation of the sensitized nanocrystal with wavelengths at the threshold of the photoabsorption spectrum. The process is initiated by an electronic excitation localized on the adosrbate molecule and is followed by interfacial electron transfer from adsorbate states mixed with the valence band of $\mathbf{Ti_{17}}$ to the electronic states of the adsorbates depleted during the primary photoexcitation event. At shorter wavelengths, however, the photoexcitation populates an electronic state that overlaps with states in the conduction band of the POT, leading to interfacial electron injection into the metal-oxide cluster. Therefore, hole injection into surface states of the POT can be achieved but only with photoexcitation wavelengths bracketed by the threshold energy of photoabsorption and the minimum energy that triggers electron injection. These findings are confirmed by measurements of negative (cathodic) photocurrents in DSSCs with a thin layer of the $\mathbf{Ti_{17}NPA_4}$ nanocrystals on FTO working electrodes, providing fundamental insights on structural and electronic factors that are critical for photoinducing cathodic mechanisms in a wide range of applications.

ASSOCIATED CONTENT

Supporting Information

Comparison of crystallographic and DFTB optimized structures for $\mathbf{Ti_{17}C343_2}$ and $\mathbf{Ti_{17}NPA_4}$. Projected DOS on Ti and O orbitals for both $\mathbf{Ti_{17}C343_2}$ and $\mathbf{Ti_{17}NPA_4}$. Atomic coordinates for $\mathbf{Ti_{17}C343_2}$ and $\mathbf{Ti_{17}NPA_4}$ DFTB optimized structures. This material is available free of charge via the Internet at http://pubs.acs.org.

AUTHOR INFORMATION

Corresponding Authors

coppens@buffalo.edu
gary.brudvig@yale.edu
victor.batista@yale.edu

Present Addresses

[‖]Centre College, Danville, Kentucky 40422, United States.
[⊥]Scotts Miracle-Gro Company, Marysville, Ohio 43041, United States.

Author Contributions

[▽]C.F.A.N. and K.J.Y. contributed equally.

Notes

The authors declare no competing financial interest.

ACKNOWLEDGMENTS

We acknowledge support by U.S. Department of Energy Grants DEFG02-07ER15909 (C.F.A.N, K.J.Y, L.J.A, R.H.C, G.W.B., and V.S.B) and DEFG02-02ER15372 (J.B.B., and P.C.). Computational work (V.S.B.) was supported as part of the Argonne-Northwestern Solar Energy Research (ANSER) Center, an Energy Frontier Research Center funded by the U.S. Department of Energy, Office of Science, Office of Basic Energy Sciences under award no. DE-SC0001059. Computer resources were provided by NERSC and by the high performance computing facilities at Yale University. M.B.O. and C.G.S. are grateful for the support by CONICET through grant PIP 112-200801-000983, PICT 2010-1233 and SECYT-UNC through grant PID 05-C627. The authors are grateful to Justin N. Nasca and David F. Watson from the University of Buffalo for useful discussions. K.N.J. gratefully acknowledges the Polish Ministry of Science and Higher Education for financial support through the "Mobility Plus" program.

REFERENCES

(1) Hagfeldt, A.; Boschloo, G.; Sun, L.; Kloo, L.; Pettersson, H. *Chem. Rev.* **2010**, *110*, 6595−6663.
(2) O'Regan, B.; Grätzel, M. *Nature* **1991**, *353*, 737−740.
(3) Young, K. J.; Martini, L. A.; Milot, R. L.; Snoeberger, R. C.; Batista, V. S.; Schmuttenmaer, C. A.; Crabtree, R. H.; Brudvig, G. W. *Coord. Chem. Rev.* **2012**, *256*, 2503−2520.
(4) Prezhdo, O. V.; Duncan, W. R.; Prezhdo, V. V. *Surf. Sci.* **2009**, *84*, 30−68.
(5) Snoeberger, R. C.; Young, K. J.; Tang, J.; Allen, L. J.; Crabtree, R. H.; Brudvig, G. W.; Coppens, P.; Batista, V. S.; Benedict, J. B. *J. Am. Chem. Soc.* **2012**, *134*, 8911−8917.
(6) Durrell, A. C.; Li, G.; Koepf, M.; Young, K. J.; Negre, C. F. A.; Allen, L. J.; McNamara, W. R.; Song, H.; Batista, V. S.; Crabtree, R. H.; Brudvig, G. W. *J. Catal.* **2014**, *310*, 37−44.
(7) Fujishima, A.; Kohayakawa, K.; Honda, J. *Electrochem. Soc.* **1975**, *122*, 1487.
(8) Odobel, F.; Le Pleux, L.; Pellegrin, Y.; Blart, E. *Acc. Chem. Res.* **2010**, *43*, 1063−1071.
(9) Nattestad, A.; Mozer, A.; Fischer, M.; Cheng, Y.; Mishra, A.; Bauerle, P.; Bach, U. *Nat. Mater.* **2010**, *9*, 31−35.
(10) Odobel, F.; Pellegrin, Y.; Gibson, E. A.; Hagfeldt, A.; Smeigh, A. L.; Hammarström, L. *Coord. Chem. Rev.* **2012**, *256*, 2414−2423.
(11) Buchalska, M.; Kuncewicz, J.; Świetek, E.; Labuz, P.; Baran, T.; Stochel, G.; Macyk, W. *Coord. Chem. Rev.* **2013**, *257*, 767−775.
(12) Gennari, M.; Legalite, F.; Zhang, L.; Pellegrin, Y.; Blart, E.; Fortage, J.; Brown, A. M.; Deronzier, A.; Collomb, M. N.; Boujtita,

M.; Jacquemin, D.; Hammarström, L.; Odobel, F. *J. Phys. Chem. Lett.* **2014**, *5*, 2254−2258.
(13) Duncan, W. R.; Prezhdo, O. V. *J. Am. Chem. Soc.* **2008**, *130*, 9756−9762.
(14) Rego, L. G. C.; Batista, V. S. *J. Am. Chem. Soc.* **2003**, *125*, 7989−7997.
(15) Abuabara, S. G.; Rego, L. G. C.; Batista, V. S. *J. Am. Chem. Soc.* **2005**, *127*, 18234−18242.
(16) McNamara, W. R.; Snoeberger, R. C.; Li, G.; Schleicher, J. M.; Cady, C. W.; Poyatos, M.; Schmuttenmaer, C. A.; Crabtree, R. H.; Brudvig, G. W.; Batista, V. S. *J. Am. Chem. Soc.* **2008**, *130*, 14329−38.
(17) De Angelis, F. *Chem. Phys. Lett.* **2010**, *493*, 323−327.
(18) Sánchez-de Armas, R.; San-Miguel, M. A.; Oviedo, J.; Márquez, A.; Sanz, J. F. *Phys. Chem. Chem. Phys.* **2011**, *13*, 1506−1514.
(19) Sánchez-de Armas, R.; Oviedo, J.; San Miguel, M. A.; Sanz, J. F. *J. Phys. Chem. C* **2011**, *115*, 11293−11301.
(20) Duncan, W. R.; Prezhdo, O. V. *Annu. Rev. Phys. Chem.* **2007**, *58*, 143−184.
(21) Li, J.; Nilsing, M.; Kondov, I.; Wang, H.; Persson, P.; Lunell, S.; Thoss, M. *J. Phys. Chem. C* **2008**, *112*, 12326−12333.
(22) Jones, D. R.; Troisi, A. *Phys. Chem. Chem. Phys.* **2010**, *12*, 4625−4634.
(23) Martsinovich, N.; Troisi, A. *J. Phys. Chem. C* **2011**, *115*, 11781−11792.
(24) Kuncewicz, J.; Zabek, P.; Kruczala, K.; Szacilowski, K.; Macyk, W. *J. Phys. Chem. C* **2012**, *116*, 21762−21770.
(25) Kuncewicz, J.; Zabek, P.; Stochel, G.; Stasicka, Z.; Macyk, W. *Catal. Today* **2011**, *161*, 78−83.
(26) Furtado, L. F. O.; Alexiou, A. D. P.; Gonçalves, L.; Toma, H. E.; Araki, K. *Angew. Chem.* **2006**, *118*, 3215−3218.
(27) Nowotny, M. K.; Bak, T.; Nowotny, J.; Sorrell, C. C. *Phys. Status Solidi B* **2005**, *242*, R88−R90.
(28) Mori, S.; Fukuda, S.; Sumikura, S.; Takeda, Y.; Tamaki, Y.; Suzuki, E.; Abe, T. *J. Phys. Chem. C* **2008**, *112*, 16134−16139.
(29) Chen, Y.; Trzop, E.; Makal, A.; Chen, Y.-S.; Coppens, P. *Dalton Trans.* **2014**, *43*, 3839−3841.
(30) Negre, C. F. A.; Fuertes, V. C.; Oviedo, M. B.; Oliva, F. Y.; Sánchez, C. G. *J. Phys. Chem. C* **2012**, *116*, 14748−14753.
(31) Oviedo, M. B.; Zarate, X.; Negre, C. F. A.; Schott, E.; Arratia-Peérez, R.; Sánchez, C. G. *J. Phys. Chem. Lett.* **2012**, *3*, 2548−2555.
(32) Elstner, M.; Porezag, D.; Jungnickel, G.; Elstner, J.; Haugk, M.; Frauenheim, T.; Suhai, S.; Seifert, G. *Phys. Rev. B* **1998**, *58*, 7260−7268.
(33) Aradi, B.; Hourahine, B.; Frauenheim, T. *J. Phys. Chem. A* **2007**, *111*, 5678−5684.
(34) Schlosshauer, M. *Decoherence, and the Quantum to Classical Transition*; Springer-Verlag: Berlin, 2007.
(35) Breuer, H. P.; Petruccione, F. *The Theory of Open Quantum Systems*; Oxford University Press: Oxford, 2002.
(36) Castro, A.; Appel, H.; Oliveira, M.; Rozzi, C. A.; Andrade, X.; Lorenzen, F.; Marques, M. A. L.; Gross, E. K. U.; Rubio, A. *Phys. Status Solidi B* **2006**, *243*, 2465−2488.
(37) Qian, X.; Li, J.; Lin, X.; Yip, S. *Phys. Rev. B* **2006**, *73*, 035408.
(38) Tsolakidis, A.; Sánchez-Portal, D.; Martin, R. M. *Phys. Rev. B* **2002**, *66*, 235416.
(39) Cheng, C.-L.; Evans, J. S.; Van Voorhis, T. *Phys. Rev. B* **2006**, *74*, 155112.
(40) Li, X.; Tully, J. C. *Chem. Phys. Lett.* **2007**, *439*, 199−203.
(41) Lopata, K.; Govind, N. *J. Chem. Theory Comput.* **2011**, *7*, 1344−1355.
(42) Morzan, U. N.; Ramírez, F. F.; Oviedo, M. B.; Sánchez, C. G.; Scherlis, D. A.; Lebrero, M. C. G. *J. Chem. Phys.* **2014**, *140*, 164105.
(43) Domínguez, A.; Aradi, B.; Frauenheim, T.; Lutsker, V.; Niehaus, T. A. *J. Chem. Theory Comput.* **2013**, 4901−4914.
(44) Oviedo, M. B.; Negre, C. F. A.; Sánchez, C. G. *Phys. Chem. Chem. Phys.* **2010**, *12*, 6706−11.
(45) Oviedo, M. B.; Sánchez, C. G. *J. Phys. Chem. A* **2011**, *115*, 12280−12285.
(46) Mukamel, S. *Principles of Nonlinear Optical Spectroscopy*; Oxford University Press: New York, 1995.
(47) Gerry, C. C.; Knight, P. L. *Introductory Quantum Optics*; Cambridge University Press: Cambridge, 2005.
(48) Bracewell, R. N. *The Fourier Transform and its Applications*; McGraw-Hill International: New York, 2000.
(49) Miller, K. J. *J. Am. Chem. Soc.* **1990**, *112*, 8543−8551.
(50) Hurum, D. C.; Gray, K. A.; Rajh, T.; Thurnauer, M. C. *J. Phys. Chem. B* **2005**, *109*, 977−980.
(51) Steunou, N.; Kickelbick, G.; Boubekeur, K.; Sanchez, C. *J. Chem. Soc., Dalton Trans.* **1999**, *0*, 3653−3655.
(52) Micic, O. I.; Zhang, Y.; Cromack, K. R.; Trifunac, A. D.; Thurnauer, M. C. *J. Phys. Chem.* **1993**, *97*, 7277−7283.
(53) Rajh, T.; Tiede, D. M.; Thurnauer, M. C. *J. Non-Cryst. Solids* **1996**, *205−207*, 815−820.
(54) Sokolow, J. D.; Trzop, E.; Chen, Y.; Tang, J.; Allen, L. J.; Crabtree, R. H.; Benedict, J. B.; Coppens, P. *J. Am. Chem. Soc.* **2012**, *134*, 11695−11700.
(55) Sato, H.; Ono, K.; Sasaki, T.; Yamagishi, A. *J. Phys. Chem. B* **2003**, *107*, 9824−9828.
(56) Fuertes, V. C.; Negre, C. F. A.; Oviedo, M. B.; Bonafé, F. P.; Oliva, F. Y.; Sánchez, C. G. *J. Phys.: Condens. Matter* **2013**, *25*, 115304.